Chapter 7

First-Principles Study of the Electron Transport Properties of Graphene-Like 2D Materials

Hui Li, Yi Zhou and Jichen Dong

Additional information is available at the end of the chapter

http://dx.doi.org/10.5772/64109

Abstract

First-principles density functional theory and non-equilibrium Green function calculations have been conducted to explore the electronic properties of the graphene-like 2D materials. It is found that zigzag boron phosphide nanoribbons (zBPNRs) exhibit non-magnetic direct bandgap semiconducting property and bandgap is about 1 eV. The heterostructure zSiC-BP-SiC nanoribbons are found to display an obvious negative differential resistance (NDR), which are tunable by changing the length of BPNRs. It is also found that for the armchair MoS_2/WS_2NRs heterostructures, with the number of WS_2NR unit cell increasing, the NDR effect can be modulated. Especially for the case of M(edge) with W atoms doping on the edges, it not only exhibits a significant NDR effect but also owns a fast current transport. Therefore, these graphene-like 2D materials may possess potential for the application in logic transistor.

Keywords: density functional theory, non-equilibrium Green function, BP nanoribbons, MoS_2 nanoribbons, heterostructure, nanoelectronics

1. Introduction

Due to the unique electronic properties and peculiar structure of graphene, such as the zero bandgap and its massless charge carriers, graphene-based nanoscale electronics and photonic devices have been attracting increasing attention [1–7]. Many researchers focused on graphene field effect transistors (FETs) as a result that FETs are the fundamental unit of the integrated circuits. Most studies have presented that graphene shows an exceptionally high carrier mobility, which enables it to easily fabricate into fast-speed FETs [8–12]. However, pristine graphene cannot been applied in the logic transistors as it does not possess a bandg-

ap, not enabling it to gain a large on/off ratio [10, 13, 14]. Therefore, for graphene, opening a sizable bandgap becomes an urgent issue, which should to be tackled by both theoretical and experimental studies. Although considerable methods have been used to solve this problem, such as chemical decorations [15–18], applying a high electric field to bilayer graphene [19–22], and cutting graphene into graphene nanoribbons (GNRs) [23–25], these methods add complexity and depress mobility. To tackle this issue, seeking other graphene-like semiconducting materials would be a better choice.

Nowadays, graphene-like materials have gained considerable research interest because they own significant advantages in low-dimensional scientific research and in nanodevice applications. In 2012, in Alejandro work, they predicted the existence of boron phosphide (BP) nanoflakes, which exhibit extraordinary electronic properties [26]. Interestingly, zigzag SiC nanoribbons (zSiCNRs) share a very similar lattice constant with zigzag BP nanoribbons (zBPNRs), but their electronic properties are different from each other. More recently, 2D transition metal dichalcogenides (TMDs), which are composed of atomic layers coupled by van der Waals forces, have gained considerable interest because of the various electronic properties that they can exhibit, for example, metallic, semiconductor, superconductor, and charge density wave [27–34]. Single-layer MoS_2, which is a semiconductor in a member of TMD family, is not like graphene but have a large bandgap. Hence, in the application of field effect transistor (FET), the MoS_2 nanoflake is a most promising candidate [35, 36]. MoS_2 monolayer consists of a Mo atom layer, which is enclosed within two S layers with hexagonal structure and these layers are held together by weakly coupled van der Waals interactions [37]. Due to such sandwich layer Mo-S-Mo structure, MoS_2 single layer could be probably fabricated repeatedly one by one from bulk materials by micromechanical cleavage [38] or exfoliation [39]. Recently, MoS_2 nanoribbons and other TMD materials with a width down to several nanometers have been synthesized [40–43]. Importantly, among these TMDs, WS_2 is expected to have similar properties with MoS_2 [44–47], and the first experimental demonstrations of monolayer WS_2 have just been reported [48]. Armchair MoS_2 and WS_2 nanoribbons have the same crystal structure and share the very similar lattice constants. Therefore, these nanoribbons might be utilized to construct heterostructures with stable coherent interfaces and multifunctionality.

2. Nanoelectronics constructed using boron phosphide and silicon carbide nanoribbons

2.1. Simulation method

All calculations were performed by the first-principles density functional theory (DFT) and the non-equilibrium Green function method with the Atomistix ToolKit software package [49, 50]. Norm-conserving pseudopotentials were used together with the double-zeta single polarized basis sets. Perdew-Burke-Ernzerhof generalized gradient approximations were employed to describe the exchange-correlation energy. The mesh cutoff was 150 Re. Monkhorst-Pack k-point was set to 1 × 1 × 50 to calculate the Brillouin zone integration. The electron

temperature of 300 K was used. The supercells of all structures were built large that vacuum layers between neighboring cells were set to at least 15 Å in order to avoid interactions between periodic images. The geometries of the devices and of the zBPNR crystal structures were optimized until the forces of the atoms were less than 0.05 and 0.01 eV $Å^{-1}$, respectively. The tolerance for energy convergence was 10^{-} eV. The device current I_d was calculated by the Landauer-Büttiker equation [49]:

$$I = \frac{2e}{h}\int_{\infty}^{-\infty} dE(T(E,V)(f_1(E) - f_2(E))) \quad (1)$$

where $T(E,V)$ represents the quantum mechanical transmission probability for electrons, $f_{1,2}(E)$ denote the Fermi functions of the source and drain electrodes, and e and h are the electron charge and the Planck constant, respectively.

2.2. Results and discussion

2.2.1. The electronics properties of zBPNRs

Figure 1a presents the structure of the hexagonal BP sheet. After optimization, B-P bond length we calculated was 1.858 Å, which is very close to the previously calculated Si-C bond length (1.787 Å) of the hexagonal SiC sheet [51]. The difference between them is less than 5%, so constructing hybrid BP-SiC structures with coherent interfaces was possible. As shown in **Figure 1c**, hexagonal BP sheet is a direct bandgap semiconductor with its highest occupied valence band maximum (HOVBM) and lowest unoccupied conductance band minimum (LUCBM) both at the k-point in the Brillouin zone. P and B atoms π states were observed both in the Bloch states of the HOVBM and the LUCBM, respectively (insets of **Figure 1a**). Moreover, it is also found that the bandgap is 0.87 eV, which is very suitable for electronic applications in FETs.

Figure 1b presents the structure of zigzag BP nanoribbons with the edges passivated by hydrogen. These nanoribbons are denoted as *N*zBPNR, in which *N* is the number of zigzag BP chains along the *y*-axis. Not like zigzag BN nanoribbons with indirect bandgaps [52], zBPNRs still maintain a direct bandgaps after cutting into nanoribbons, where the HOVBM and LUCBM are both located at the K_M point in the Brillouin zone (**Figure 1d**). **Figure 1d** also shows that both the HOVB and the LUCB have a noticeable flat component between the K_M point and the K_Z point, different from others. We can see from **Figure 2a** that the HOVBM of the 6zBPNR locates only at the P atoms, the eigenstates of which diminishes from the P to B edge gradually(left panel), while the HOVB at the K_Z point only locates at the P atoms of P edge. Likewise, as shown in **Figure 2b**, the LUCBM and the LUCB at the K_Z point shares the same trend but

the eigenstates locates at the B atoms. Therefore, their edge states should have a great effect on the bandgaps of zBPNRs calculated from HOVBM and LUCBM.

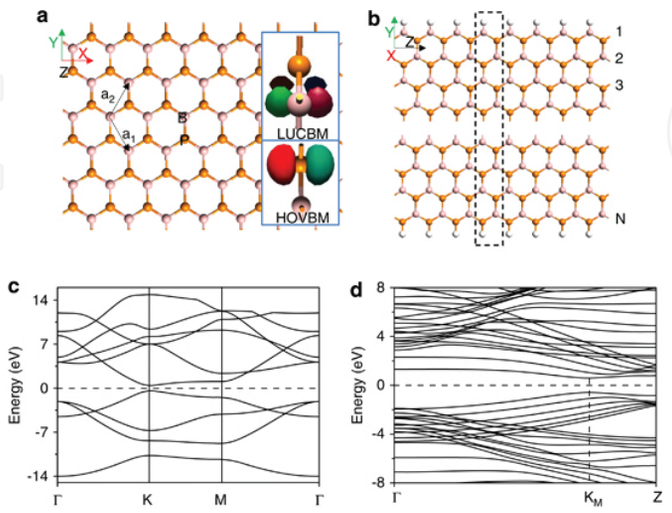

Figure 1. Structures of (a) the hexagonal boron phosphide (BP) sheet and (b) the zigzag boron phosphide nanoribbons (zBPNRs). The arrows and the dashed box denote the unit cell. Band structures of (c) the BP sheet and (d) the 6zBPNR. The light color represents B atom and another one is P atom.

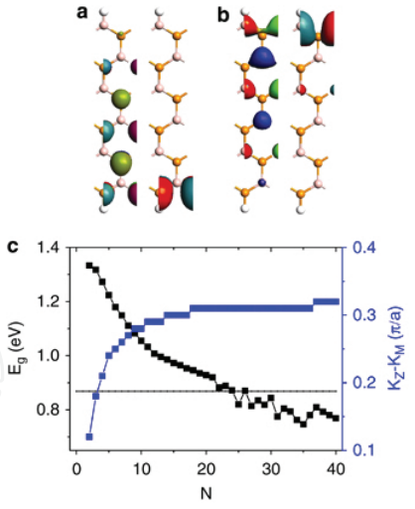

Figure 2. The Bloch states (a) at the highest occupied valence band maximum (HOVBM; left panel) and the HOVBK_Z (right panel), and (b) at the lowest unoccupied conductance band minimum (LUCBM; left panel) and the LUCBK_Z (right panel). The isovalue is 0.1. (c) The variation in the bandgap and the K_z - K^M of zigzag boron phosphide nanoribbons (zBPNRs) with the increase of the ribbon width.

To understand whether the width of the ribbon has effect on the bandgaps (E_g) of zBPNRs, we study the relationship between E_g and N, as shown in **Figure 2c**. Evidently, the E_g dropped monotonously as the ribbon width N increased from 2 to 21. Further increasing N to 40, the E_g

http://dx.doi.org/10.5772/64109

decreases slowly and displays the trend of fluctuation. Moreover, compared to the bandgaps of the BP sheet, when N exceeded 24, E_g of zBPNRs became lower than that which cannot be explained by the quantum confinement effect. As a matter of fact, the above-mentioned phenomena can be explained by two factors, one of which is the electrons transfer between B and P atoms, and the other is the screening effect from the inner part of the ribbon. Because of the different electronegativities of B and P, an electric field and the screening effect can be formed spontaneously when the electron transfers between the two edges of the zBPNRs. As shown in **Figure 2c**, when N increased, the distance between the K_M point and the K_Z point increases and fewer electrons were accumulated at the edges. Therefore, the energy at the B edge decreased and the energy at the P edge increased simultaneously, resulting in the decrease of bandgaps. As the width of the ribbon was sufficiently large and N exceeds 24, we can see from **Figure 2c** that the bandgap fluctuates because of the screening effect emerging to compete with the electron transfer effect. From the above discussion, it can be concluded that zBPNRs may possess potential for applications in optotronics and logic electronics.

2.2.2. Hybrid zSiC-BP-SiC nanoribbon devices

Previous studies have shown that the ferrimagnetic state of the 6zSiCNR is a semiconductor with a very small bandgap, while the non-magnetic state of the 6zSiCNR is also a semiconductor with a negligible bandgap and the energy difference between the states of them is very small [53]. Meanwhile, the spin-polarized state would become unstable when external fields are applied [54]. Therefore, we employ a spin-unpolarized calculation to investigate the electron transport properties of the in-plane zigzag SiC and BP(zSiC-BP-SiC) nanoribbon heterostructures. **Figure 3a** shows a structure of such heterostructures, which consists of the scattering region, a hybrid zSiC-BP-SiC structure, and source and drain electrodes, denoted

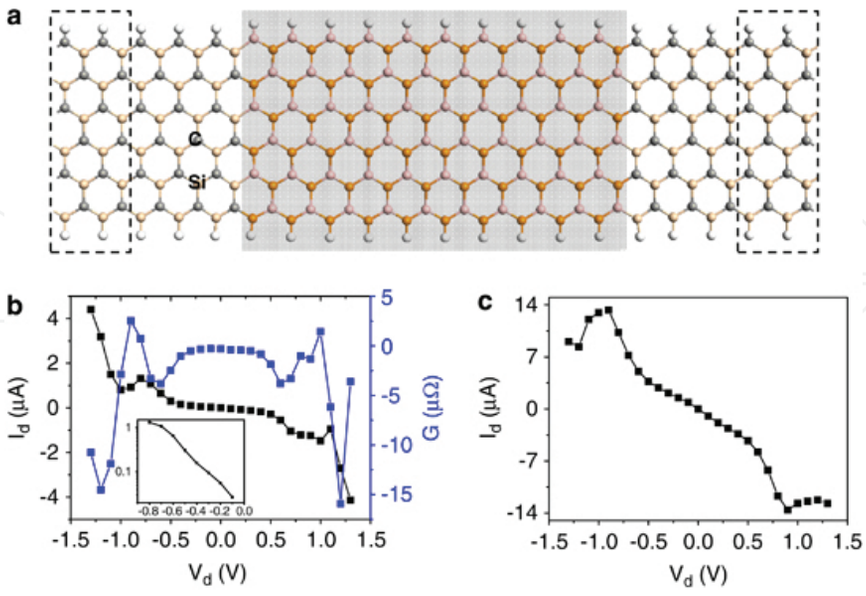

Figure 3. (a) The structure of a zSiC-BP-SiC nanoribbon heterostructure. (b) I_d-V_d and conductance curves of this heterostructure. The inset shows the lgI_d-V_d curve. (c) I_d-V_d curve of a zSiC-BP-SiC nanoribbon heterostructure with a shorter zigzag BP nanoribbon (zBPNR).

by dashed boxes. We study the current-voltage characteristics of this heterostructure, as shown in **Figure 3b**. An obvious non-linear feature was found, due to the discrete energy levels of the nanomaterial. Furthermore, from the I_e-V_d curve, we can see that this heterostructure exhibited a significant conductance gap, resulting from the semiconducting property of the zigzag BP nanoribbons. More interestingly, an obvious NDR effect appeared asymmetrically in the I_d-V_d curve, being at the bias of −0.8 and 1 V, respectively. The asymmetry of the current-voltage characteristics was obviously caused by the asymmetric structure of the scattering region. Further analysis showed that NDR effect could be affected by the width of the BP nanoribbons.

To understand the physical mechanism appearing at the electron transport properties of this heterostructure, transmission spectrum and local density of states (LDOS) [55] at different voltage should be calculated, as shown in **Figure 4**. The LDOS was averaged in the *x*-*y* plane and colored with red and blue, indicating large and small density areas, respectively. In **Figure 4a**, we can see that when there was no bias, the corresponding transmission spectrum exhibited an obvious transmission energy gap, about 0.7 eV around the Fermi level, which was consistent with the current-voltage curves and came from the semiconducting property of the zBPNR, suggesting that such heterostructures have potential applications in FETs [56]. Moreover, a very small transmission peak appeared at the E_f, as shown in the inset of **Figure 4a**, which played an important role in the NDR effect as mentioned above. This small transmission peak was generated by the quantum tunneling effect of electrons between the two zSiCNRs which were located at the two sides of the zBPNR. As shown in **Figure 4d**, the local DOS at the E_f mainly originated from the region of zSiCNR and the SiC-BP interfaces, while there was no electron state at the zBPNR region. As a result, electrons at the E_f were only

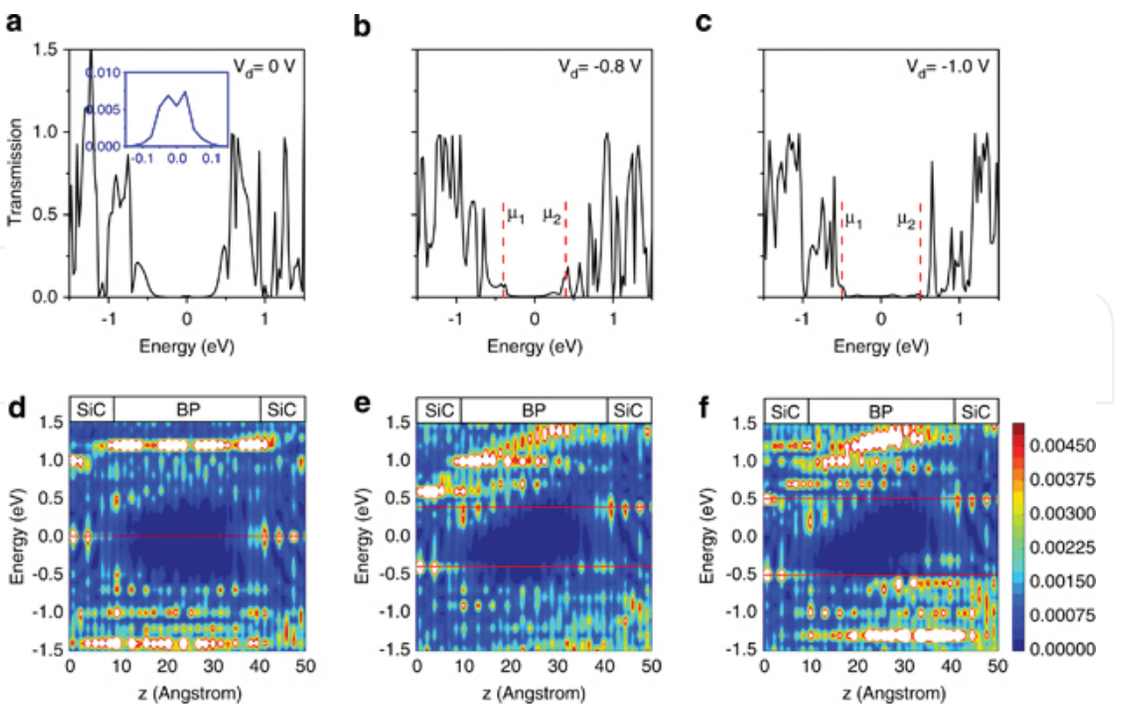

Figure 4. (a-c) Transmission spectrum and (d-f) the local density of states of the heterostructure as shown in **Figure 3(a)** at the bias of 0, −0.8, and −1.0 V, respectively.

able to penetrate the scattering region via the tunneling effect. When the bias decreased from 0 to −0.8 V, as shown in **Figure 4b**,the transmission spectrum went into the bias window, and in the mean time, the transmission of electrons by the tunneling effect at −0.4 eV was increased, which was demonstrated by the LDOS in **Figure 4e** that the states at that energy was enhanced. The transmission spectrum changes in the energy window resulted in a dramatic increase of the current, as shown in the inset of **Figure 3b**. Further decreasing the voltage to −1.0 V, the electron transmission spectrum in the energy window inclined (**Figure 4c**) and the NDR effect appeared, which could be explained that the electron transmission mechanism began to transform from pure tunneling effect to resonant tunneling effect. We can deduce from the above analysis that it is possible to control the tunneling effect. And the NDR effect could also be changed by changing the width of zBPNR. As indicated in **Figure 3c**, the current-voltage curve of a zSiC-BP-SiC nanoribbon heterostructure with a shorter zBPNR consisting of six periodic units clearly showed that the tunneling current was considerably larger than the one discussed above with a longer zBPNR. More importantly, an obvious NDR effect could be also observed in this heterostructure with a shorter zBPNR, and the bias of the current peak asymmetrically located at ±0.9 V, which indicated that the NDR effect of such zSiC-BP-SiC heterostructure could be controlled by the width of zBPNR. As a matter of fact, C_{60}-based structures also exhibited a similar NDR effect, but these structures are much more difficult to be fabricated and may become unstable owing to complicated interface coupling [57].

2.2.3. Diode-like structure constructed using zBP-SiC nanoribbons

We also studied the electron transport properties of a diode-like structure consisting of the zigzag BP and SiC nanoribbons, denoted as zBP-SiC. The current-voltage curve of a 5zBP-SiCdiode-like device was shown in **Figure 5**. Due to the semiconducting property of the zigzag BP nanoribbons, we can see there was no current appearing until the bias of ±0.5 V in the current-voltage curve. In addition, when the bias of ±1 V was applied, 5zBP-SiC diode-like device exhibited a slight NDR effect. We can see from the transmission spectrum and the LDOS under different bias that such NDR effect also originated from the change in coupling between the zigzag BP and SiC nanoribbons, as shown in **Figure 6**. As a result, in **Figure 6e**, as the

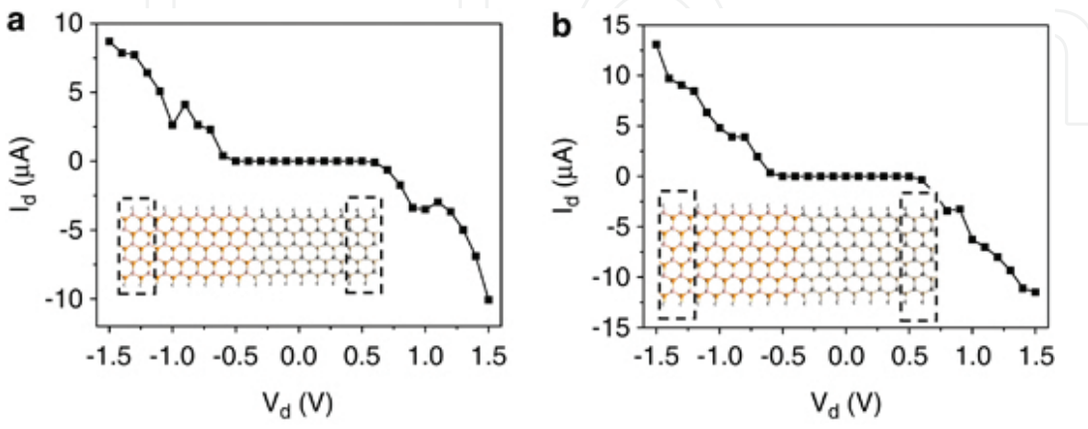

Figure 5. (a) I_d-V_d curve of the 5zBP-SiC two-probe device, and (b) I_d-V_d curve of the 6zBP-SiC two-probe device. The insets are the structures of these devices.

applied bias is −0.9 V, electrons of the lowest unoccupied molecular orbital of the zBPNR contributed to the increase of the current and the electrons of SiC flowed through both the highest occupied molecular orbital and the lowest unoccupied molecular orbital. However, when further decreasing the bias to −1.0 V, we can see from **Figure 6c** and e that the contribution of the highest occupied molecular orbital of the zSiCNR moving away from the bias window and the current was significantly depressed, leading to the decrease of the current in **Figure 5a**. In **Figure 5b**, we also study the current-voltage curve of this diode-like device with a wider width, which showed that NDR effect weakened and disappeared as the width of the ribbon increased.

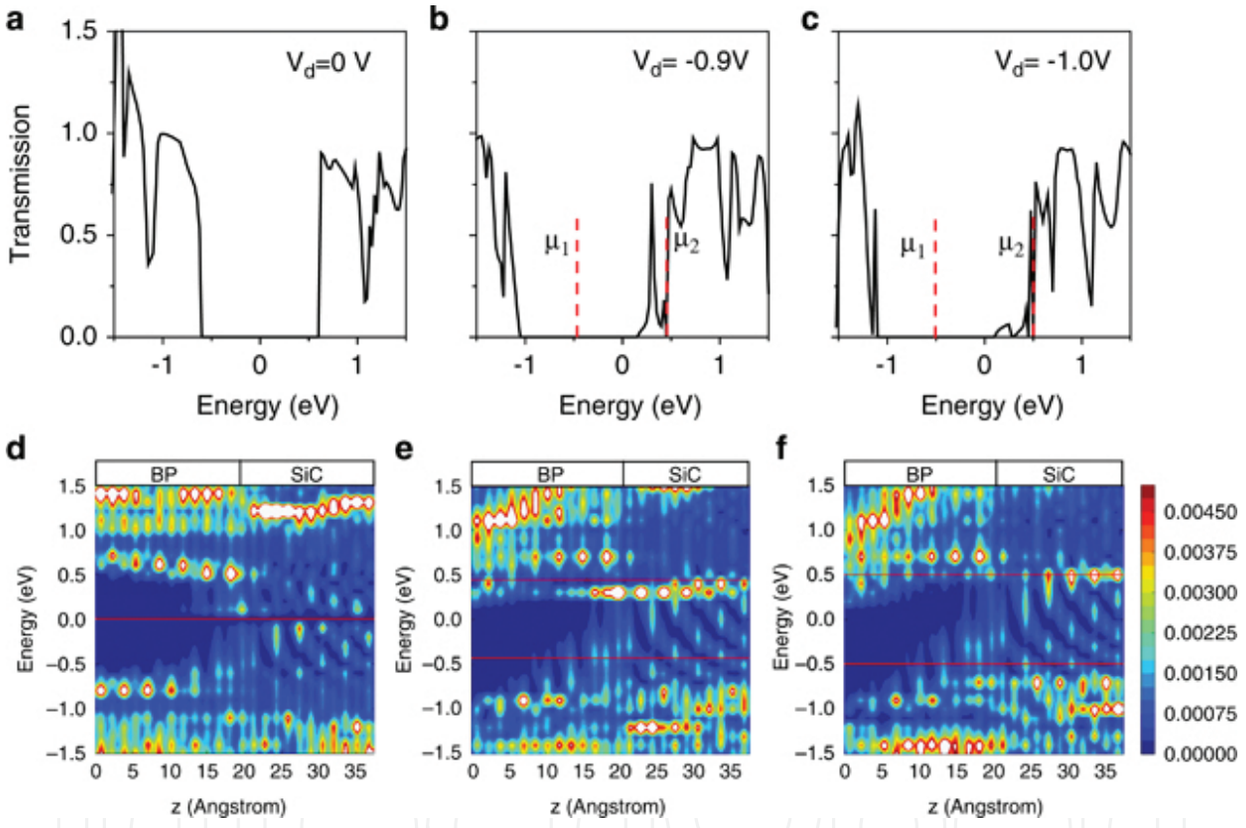

Figure 6. (a-c) Transmission spectra, and (d-f) local density of states of the two-probe device shown in **Figure 5(a)** at V_d of 0, −0.9, and −1.0 V, respectively.

To investigate whether the zBPNRs played an important role in the heterostructures mentioned above, we investigate the electron transport properties of folded 4zSiCNRs, as shown in **Figure 7**, with the overlapping area decreasing from device a to d. The transmission spectrum of the four cases indicates that there was no transmission energy gaps near the Fermi energy, because the non-magnetic 4zSiCNR is a narrow-gap semiconductor. As mentioned above, it is concluded that only the zSiCNR structure is difficult to construct into nanoelectronics.

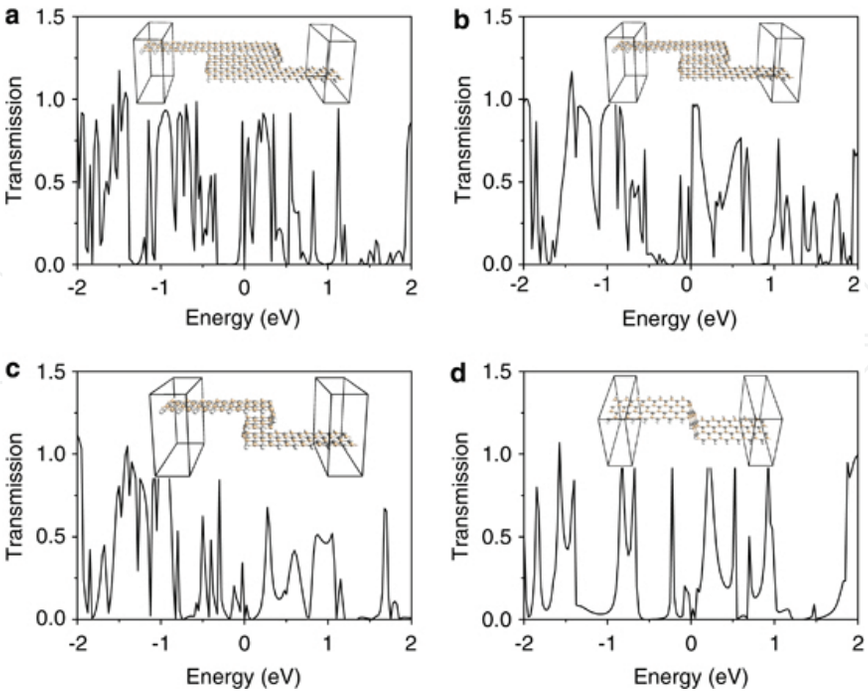

Figure 7. Transmission spectra of fourfold 4zSiCNR (silicon carbide nanoribbon) two-probe devices. The insets illustrate the corresponding structures of these devices.

3. In-plane heterostructures constructed using MoS_2 and WS_2 nanoribbons

3.1. Simulation method

All calculations were performed by the first-principles density functional theory (DFT) and the non-equilibrium Green function method with the Atomistix ToolKit software package [49, 50]. Norm-conserving pseudopotentials were used together with the double-zeta single polarized basis sets. Perdew-Burke-Ernzerhof generalized gradient approximations were employed to describe the exchange-correlation energy. The mesh cutoff was 150 Re. Monkhorst-Pack k-point was set to 1 × 1 × 100 to calculate the Brillouin zone integration. The electron temperature was employed by 300 K. The supercells of all structures were built large that vacuum layers between neighboring cells were set to at least 15 Å in order to avoid interactions between periodic images. The geometries of the devices and of the crystal structures were optimized until the forces of the atoms were less than 0.05 and 0.01 eV $Å^{-1}$, respectively. The tolerance for energy convergence was 10^{-5} eV. The device current d_d was calculated by the Landauer-Büttiker equation [49]:

$$I = \frac{2e}{h}\int_{\infty}^{-\infty} dE(T(E,V)(f_1(E) - f_2(E))) \tag{2}$$

where $T(E,V)$ represents the quantum mechanical transmission probability for electrons, $f_{1,2}(E)$ denote the Fermi functions of the source and drain electrodes, and E and h are the electron charge and the Planck constant, respectively.

3.2. Results and discussion

Figure 8 shows the devices consisting of an armchair MoS_2NRs/WS_2NRs heterostructure. The devices are placed along the z direction, and the x-axis is perpendicular to its surface. The two-probe device consists of two parts, which are the scattering region, making of MoS_2NRs/WS_2NRs heterostructure, and source and drain electrodes, the supercells of which are denoted in yellow box. And these heterostructures are described by M(na) and M(nz), where n indicates the width of the WS_2NR in the scattering region, and a(z) denotes the armchair or zigzag-shaped ribbon.

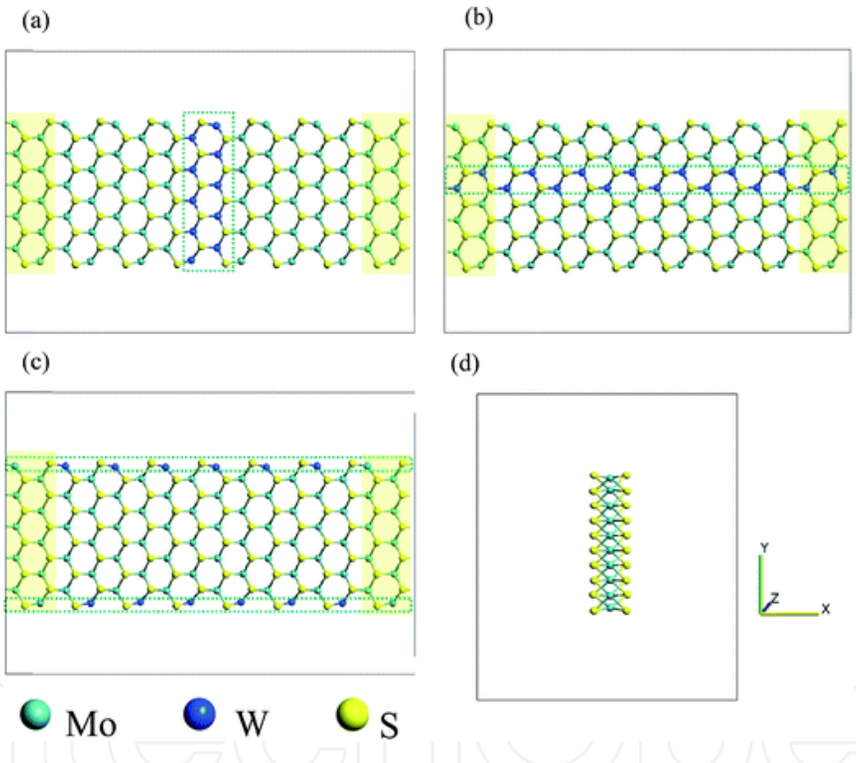

Figure 8. Structure of MoS_2NR/WS_2NR heterostructure two-probe devices. Dashed box denotes the contacting WS_2NR. The supercells of the devices are marked by solid rectangle. (a) Structure of M(1a) two-probe device. (b) Structure of M(1z) two-probe device. (c) Structure of M(edge) two-probe device. (d) Side view of these heterostructures.

3.2.1. Heterostructure of WS_2/MoS_2 with zigzag direction interface

In Gong et al. [58] work, they found that in-plane heterostructure of zigzag direction interface between WS_2 and MoS_2could be mostly appeared in the MoS_2/WS_2 hybrid structures. Therefore, we first construct M(na) with the interfaces along the zigzag directions, in other words, MoS_2NRs and WS_2NRs are arranged in perpendicular. And the electron transport properties of these heterostructures are investigated. The current-voltage curves of M(na) are presented

http://dx.doi.org/10.5772/64109

in **Figure 9** with WS_2NRs lengths n ranging from 1 to 3. It can be clearly seen that no matter the length of the WS_2NRs, all the three cases exhibit an obvious conductance gap in the current-voltage curves before the bias of 0.6V, which results from the semiconducting property of the armchair MoS_2 nanoribbon. Moreover, on further increasing the bias, these heterostructures all exhibit a significant NDR effect, which locate at 0.9 V bias. As indicated from **Figure 9**, the WS_2NR length has impact on the NDR effect, with the length of WS_2NR increasing, the current is enhanced more quickly and M(3a) owns the most current peak among these two-probe devices. In addition, peak-to-valley ratio (PVR) that represents the extent of the NDR effect also increases, namely 3.01, 4.931, and 5.441, respectively, and the NDR window are the same, that is, 0.1 V. It is concluded that it exhibits a relatively good NDR performance when contacting more unit cells of WS_2NRs. From the above discussion, it indicates that these heterostructures may possess the potential for application of logic transistor.

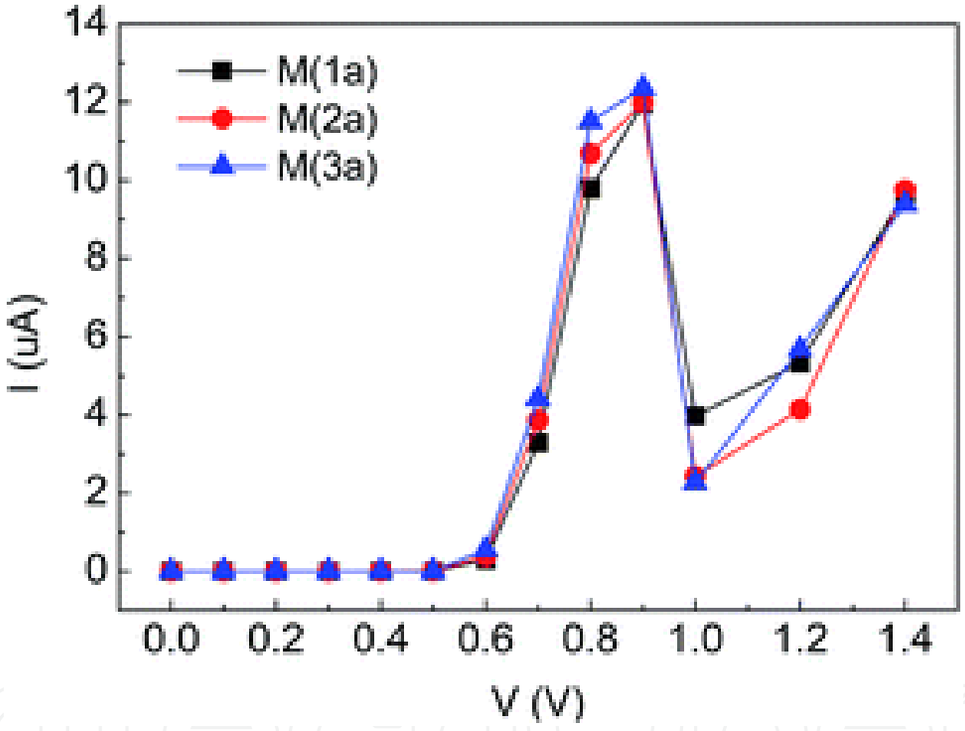

Figure 9. I_d-V_d curves of M(na) with WS_2NR length n ranging from 1 to 3.

We now investigate the physical origin of the NDR; the transmission spectrum is shown in **Figure 10(a)** for M(3a) at several typical bias voltages. When a small bias of 0.6 V is applied, a little transmission peak occurs in the transmission energy window and spontaneously the current begins to appear initially. Further increasing the bias to 0.9 V, the transmission peak under the bias window broadens, resulting in the increase of current and up to the maximum current. Interestingly, as applied the bias to 1.0 V, the height of transmission peak drops largely, which play the most dominant contribution to the current. Although there are additional two small peaks appearing in the bias window, the negative contribution to the current can be

ignored. Therefore, the NDR effect can be found in the **Figure 8**. And when the bias continuously increases to 1.4 V, the transmission peaks under the expanding bias window increase and broaden, which results in a steady increase in current. In **Figure 10(b)** and **(c)**, to explain whether the NDR effect of these three heterostructures is different from each other, transmission spectrum at bias of 0.9 and 1.0 V is calculated. In the case of the applied bias of 0.9 V, all the cases have the single peak under the bias window. However, when the length of the WS_2NR enlarges, the height of transmission peak also increases but slowly, such that the current peak of these cases has a small increase, while for the cases of 1.0 V bias, with *n* increasing from 1 to 3, the majority of peaks under the bias window decrease. However, there is another small transmission peak exhibiting an opposite trend, but the contribution to the current is ignored. Therefore, when the length of the WS_2NR decreases, the current valley decreases simultaneously in **Figure 9**. And from **Figure 10(b)**, we can also investigate the reduction extent which is consistent with variation of the current-voltage curves that as the length of the WS_2NR *n* increases from 1 to 2, the degree of reduction of transmission peaks denoted by b and c performs more significantly than when it increases from 2 to 3.

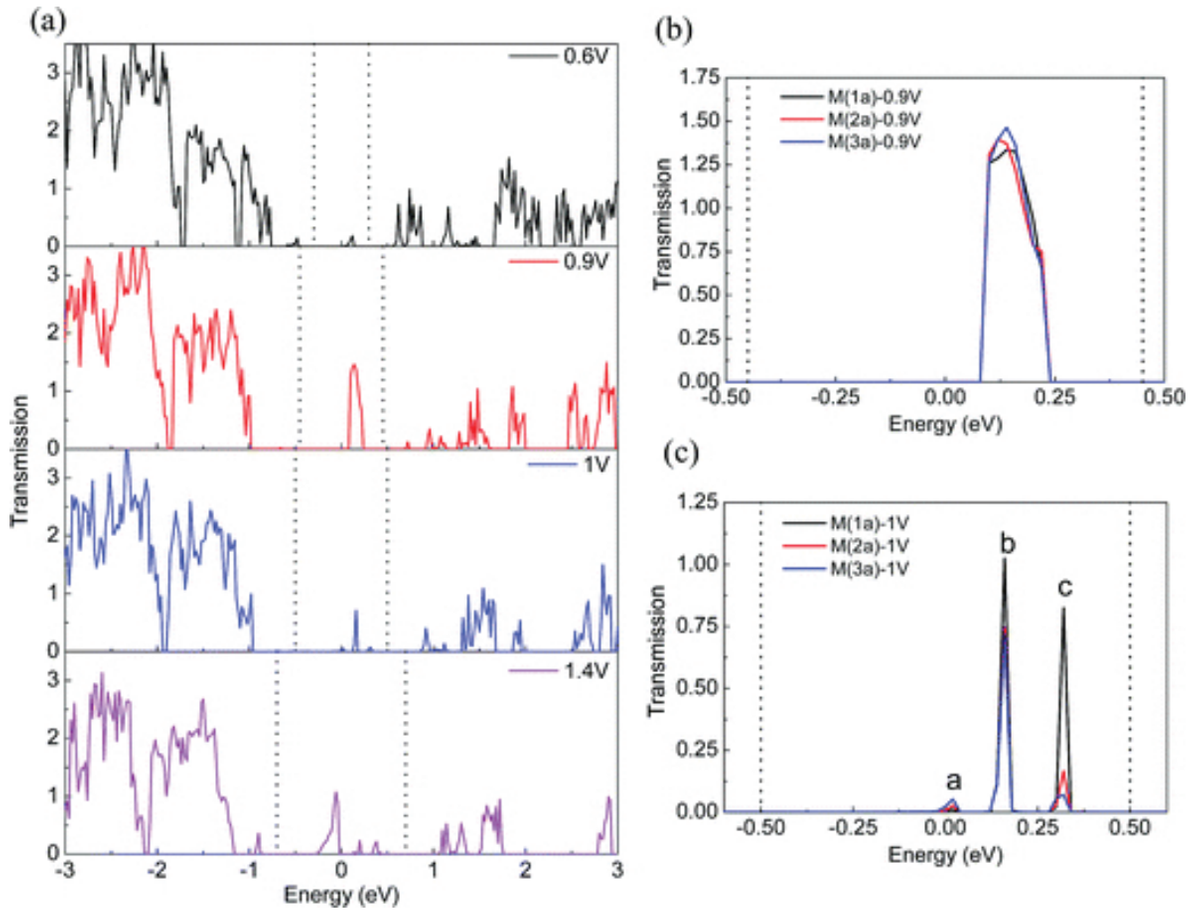

Figure 10. Transmission spectrum (a) for M(3a) at four typical biases, and for M(*n*a) (b) at the bias of 0.9 V and (c) at the bias of 1.0 V as the WS_2NR length *n* ranges from 1 to 3. Dotted line represents the bias window.

http://dx.doi.org/10.5772/64109

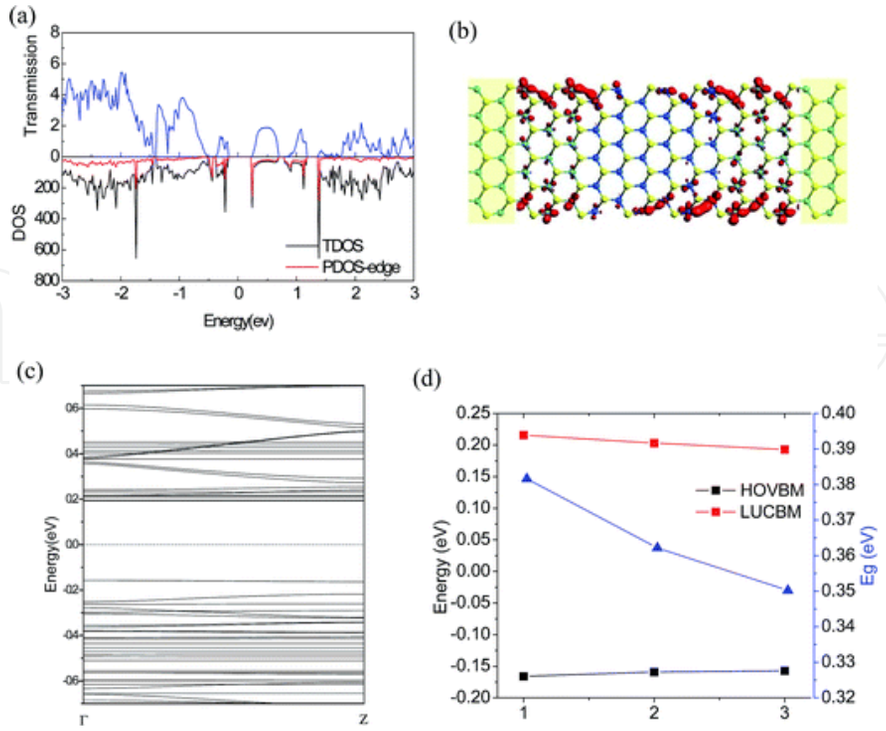

Figure 11. (a) Equilibrium transmission spectrum, and total and projected density of states for M(3a), (b) LDOS at E_f −0.18 eV with an isovalue of 0.1, (c) band structures for M(3a), and (d) HOVBM, LUCBM, and bandgap for M(*n*a) as the WS_2NR length *n* ranges from 1 to 3.

To identify the nature states of the electron transport properties, equilibrium density of states (DOS) of these devices and their corresponding band structure of crystal structures are calculated and shown in **Figure 11**. In **Figure 11(a)**, the curve of DOS indicates that zero electron states occur at E_f because of the semiconductor characteristics of armchair MoS_2 and WS_2 nanoribbons, not resulting in electron transmission at E_f, which correspond to current-voltage curves (**Figure 9**) that there is a conductance gap before the bias of 0.6 V. In addition, the changes of transmission peaks around E_f can be explained directly by the DOS. Interestingly, the projected density of states on the edge (PDOS edge) is mainly consistent with the total density of states (TDOS) in the energy range from −0.4 to 1.2 eV, indicating that the states from the edges contribute to the electrons through the scattering region near E_f. Besides, to describe this phenomenon clearly, we also calculate the local density states (LDOS) at −0.18 eV, as shown in **Figure 11(b)**. It can be clearly seen that at that energy, the electron states originate from the W and Mo atoms on the two edges. Moreover, as the WS_2NR length increases, the electron states are enhanced and becomes bigger and bigger. From the above discussion, it can be concluded that electrons are prone to transport the scattering region from the edges of transition metal atoms with a higher energy, which can be explained by the effect of dangling bonds. From the analysis of the band structure, we can see that armchair MoS_2/WS_2NRs heterostructures remain as a direct bandgap semiconductor with its highest occupied valence band maximum (HOVBM) and lowest unoccupied conductance band minimum (LUCBM) both at Γ point in the Brillouin zone, as shown in **Figure 11(c)**, which indicates that the good optical characteristics of MoS_2 retain in the armchair MoS_2/WS_2NRs heterostructures. The

above discussion means that MoS_2/WS_2NRs heterostructures may possess potential for their application in optotronic devices. The information regarding the changes of LUCBM and HOVBM among these heterostructures is shown in **Figure 11(d)**. With the length of WS_2NRs increasing, the bandgaps decline, which results from the decrease of LUCBM and the increase of HOVBM. Although there are changes in the bandgaps of these heterostructures, when the bias is applied, the current increases more quickly with a higher current peak in **Figure 9**. The variation of the bandgap we observed is consistent with Gong et al. [58] work that the PL peak position shifted continuously across the interface.

3.2.2. Heterostructure of WS_2/MoS_2 with armchair direction interface

In addition, as Gong et al. [58] work mentioned, besides the preferred zigzag interface, in-plane heterostructures of $WS_2/MoS_2$with the armchair interface were also occasionally observed. Therefore, we also study the electron transport properties of such armchair MoS_2/WS_2NR heterostructures with the interface along the armchair direction with the increasing length of WS_2NR. In **Figure 12**, the current-voltage curves of M(*n*z) with *n* ranging from 1 to 4 are presented. Apparently, these heterostructures all exhibit significant NDR effect, located at the applied bias from 0.9 to 1.0 V. Moreover, in the case of M(4z), another NDR effect is observed at the bias of 1.2 V with an ignored PVR. All these heterostructures own the same NDR window, that is, 0.1 V. When the width of WS_2NR increasing from 1 to 4, the NDR effect is depressed and PVR is 3.3037, 2.7585, 1.6063, and 1.003, respectively. Especially for M(4z), the NDR effect is the most inferior, but the current increases more significantly than the other cases. From the above discussion, it is concluded that these hybrid two-probe devices may not be a good candidate for the application in logic transistor.

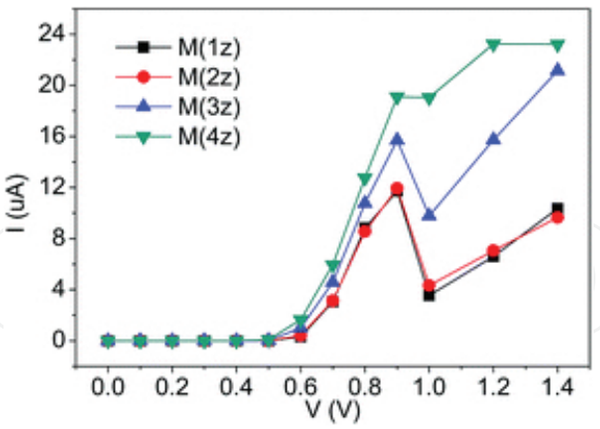

Figure 12. I_d-V_d curves of M(*n*z) with WS_2NR length *n* ranging from 1 to 4.

To understand the observed NDR effect, it is useful to analyze the evolution of the transmission spectrum as the bias potential is ramped up for M(1z) and some typical biases are shown in **Figure 13(a)**. When a small bias of 0.6 V is applied, transmission peak begins to appear in the bias window, which results in an increase in the current. Under the bias of 0.9 V, only one transmission peak appeared in the bias window and peak height gradually enhances as the

bias is applied. Simultaneously, the weight of the transmission spectrum in the bias window is enlarged, leading to the increase of current. When the bias is 1.0 V, an additional transmission peak appears in the expanding bias window, but the only peak in the bias window of 0.9 eV drops significantly. Compared to each other, the height of peak reduction outweighs another small peak appearing in the bias window, resulting in the decrease of current. As a result, current-voltage curves exhibit the NDR effect (**Figure 12**). When further increasing the bias to 1.4 V, the transmission peaks in the bias window broaden and there are some small peaks moving into the extending bias window, leading to a steady increase in the current. For the case of M(4z), with a wider WS_2NR, transmission spectrum at some several typical biases is presented in **Figure 13(b)**. It is more obvious that the initial transmission peak appears in the bias window and with the bias increasing, the height of the peak enhances. When the bias exceeds 0.9 V, the contribution of transmission spectrum both at the bias of 1.0 and 1.4 V under the bias window all decrease slightly, leading to twice NDR effect with the ignored PVR. In **Figure 13(c)** and **(d)**, we study the distinction of these four heterostructures, and transmission spectra at bias of 0.9 and 1.0 V are calculated. When the width of WS_2NR increases from 1 to 4, the transmission peaks both at two biases broaden and therefore both the current peak and valley increase. After investigating the variation of PVR, we find that as the width of WS_2NR broadens, the increasing extent for bias of 1.0 V is more obvious than the bias of 0.9 V. From the above discussion, it is explained the reason why the NDR effect is depressed.

To investigate the mechanism of the electron transport properties, we calculate the equilibrium TDOS and PDOS on the edges of M(1z), as shown in **Figure 14(a)**. It can be seen that a significant electron state gap appear around E_f in the DOS, which results from the semiconducting feature of armchair MoS_2 nanoribbons. Moreover, it directly corresponds to the transmission spectrum that there is also an obvious transmission gap occurring. Interestingly, the projected density of states on the edge (PDOS-edge) is mainly consistent with the TDOS around Fermi level, indicating that the states from the edges contribute to the electrons through the scattering region. Besides, to describe this phenomenon clearly, we also calculate the local density states (LDOS) at −0.18 eV, as given in **Figure 14(b)**; it can be clearly seen that at the energy of −0.18 eV, the electron states originate from the Mo atoms on the two edges. In other words, electrons transport through the scattering region mainly from the transition metal atoms of the edge. As discussed earlier, because the Mo atoms on the edges have higher energy with unfilled d orbit, the electron can easily transport from them. Moreover, band structure of the crystal is analyzed in **Figure 14(c)**. From the analysis of the band structure, we can see that these four heterostructures exhibit a direct bandgap semiconducting property with HOVBM and LUCBM both at Γ point in the Brillouin zone, as shown in **Figure 14(c)**. The optical characteristics of armchair MoS_2 nanoribbons do not change after being in contact with WS_2, and these hybrid two-probe devices may also possess the potential application in optotronics. To clearly investigate the variation of the bandgaps among these heterostructures, we extract the information in **Figure 14(d)**. When the width of WS_2NR increases, there is a slight decrease in bandgap, resulting from the decrease of LUCBM and the increase of HOVBM. Therefore, more electrons can jump from HOVBM to LUCBM easily and as the bias is applied, the current increases more quickly with a higher current peak. Moreover, Gong et al. [58] work confirms our finding that the PL peak position shifted continuously across the interface.

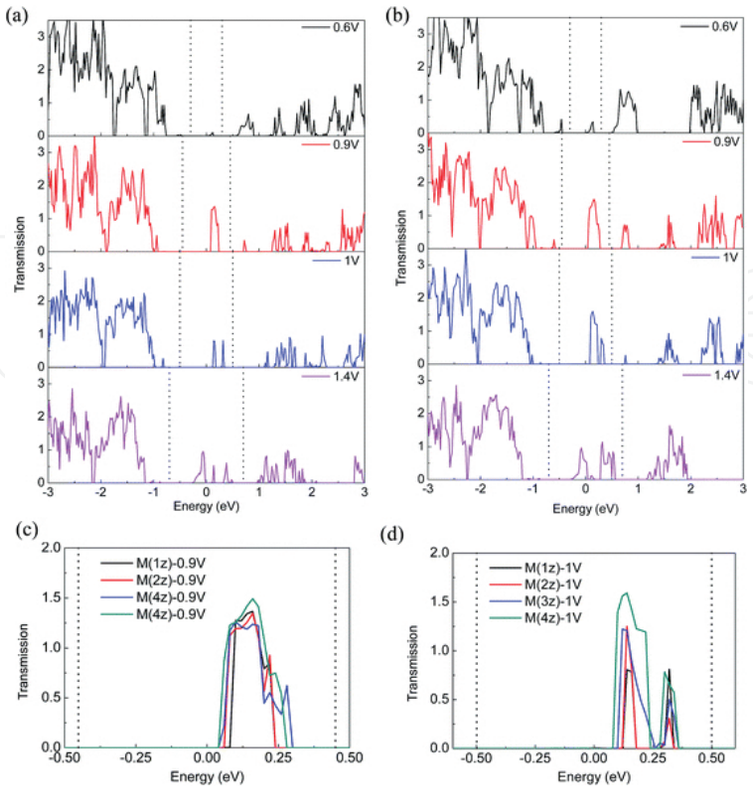

Figure 13. Transmission spectra for (a) M(1z) and (b) M(4z) at four typical biases. Dotted line represents the bias window. Transmission spectra for M(*n*z) (c) at 0.9 V bias and (d) at 1.0 V bias as width of WS_2NR *n* ranges from 1 to 4.

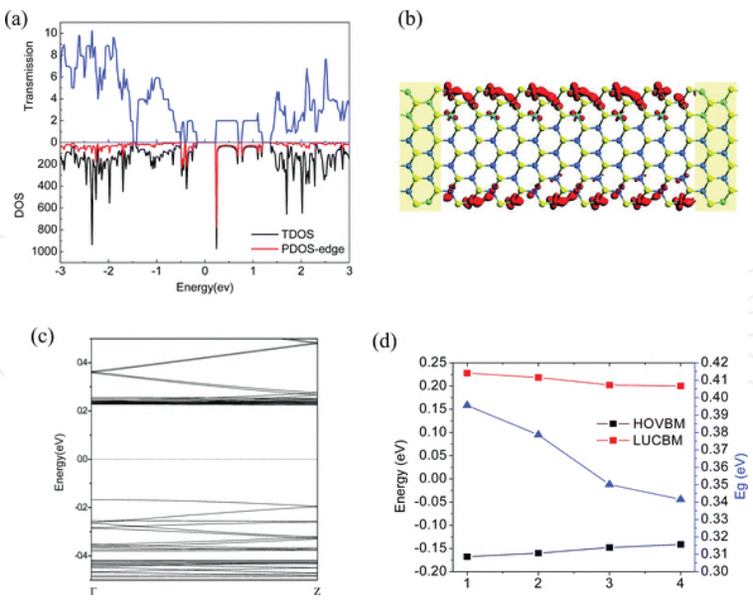

Figure 14. (a) Equilibrium transmission spectrum, total and projected DOS, (b) LDOS at E_f −0.18 eV with an isovalue of 0.1, (c) band structures of M(1z), and (d) HOVBM, LUCBM, and bandgap for M(nz) as the length of WS_2NR *n* ranges from 1 to 4.

http://dx.doi.org/10.5772/64109

3.2.3. MoS_2/WS_2 heterostructure with W atoms doping on the edges

Lastly, we study the another heterostructure denoted by M(edge) that Gong et al. [58] did not discuss, in which the Mo atoms on the edges are replaced by W atoms. Due to the same amount of W doping, M(1z) makes a comparison with this heterostructure to investigate whether edge states influence electronic transport properties. In **Figure 15**, we calculate current-voltage curves for M(edge). Compared to M(1z), a significant NDR effect also appears in M(edge), but the NDR window enlarges to 0.3 V. When the bias exceeds 0.6 V, an initial current appears and increases more rapidly than the case of M(1z), and then the current continues to enhance up to its maximum at 0.9 V. Although the current peak is almost similar to the case of M(4z), there is a lowest current valley among these heterostructures, which leads to the best NDR effect and largest PVR is 18.4462. Interestingly, M(edge) and M(1z) are doped the same amount of W atoms. However, the M(edge) performs more excellently than M(1z) and exhibits a better NDR effect and the faster current transport. In fact, this phenomenon can be explained that the W atoms on the edge possess the higher energy, resulting in the electrons of W atoms easily transporting through the edges than from the inside. From the previous discussion, M(edge) exhibits not only a significant NDR effect but also a fast current transport, which would make it the best candidate in the application of logic transistor.

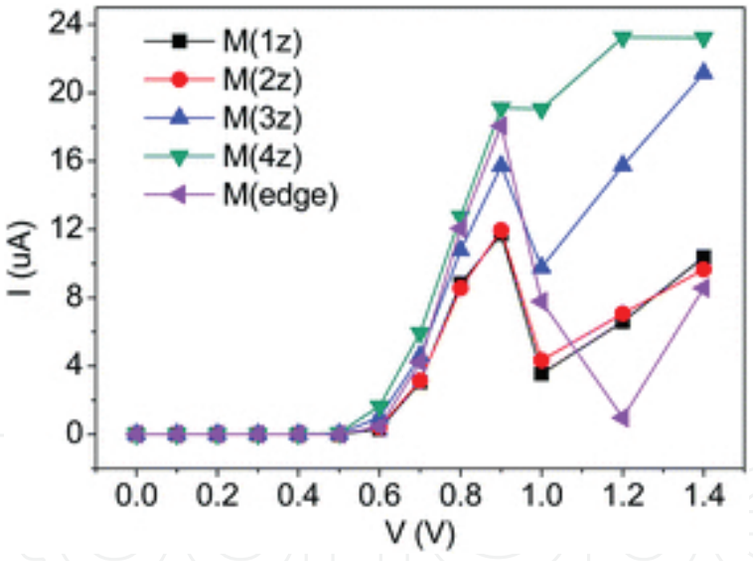

Figure 15. I_d-V_d curves of M(edge) and M(nz) with WS_2NR length n ranging from 1 to 4.

To understand the observed NDR effect, transmission spectra at four typical biases are calculated, as shown in **Figure 16(a)**. When applied a small bias of 0.6 V, the transmission energy window occurs a little transmission peak, resulting in an initial current. When the bias is 0.9 V, the single transmission peak in the bias window broadens up to its maximum. Further increasing the bias, this only transmission peak reduces obviously into two small peaks. Therefore, it displays a significant NDR effect. To clearly investigate the distinction between the M(1z) and M(edge), we calculate the transmission spectrum at the bias of 0.9, 1.0, and 1.2 V, respectively, as shown in **Figure 16(b-d)**. For the bias of 0.9 and 1.0 V, the transmission

spectrum of M(edge) contributes larger than M(1z) in the bias window and results in a higher current. However, in the case of 1.2 V bias, for M(edge), the height of two peaks under the bias window are both lower, resulting in a small current.

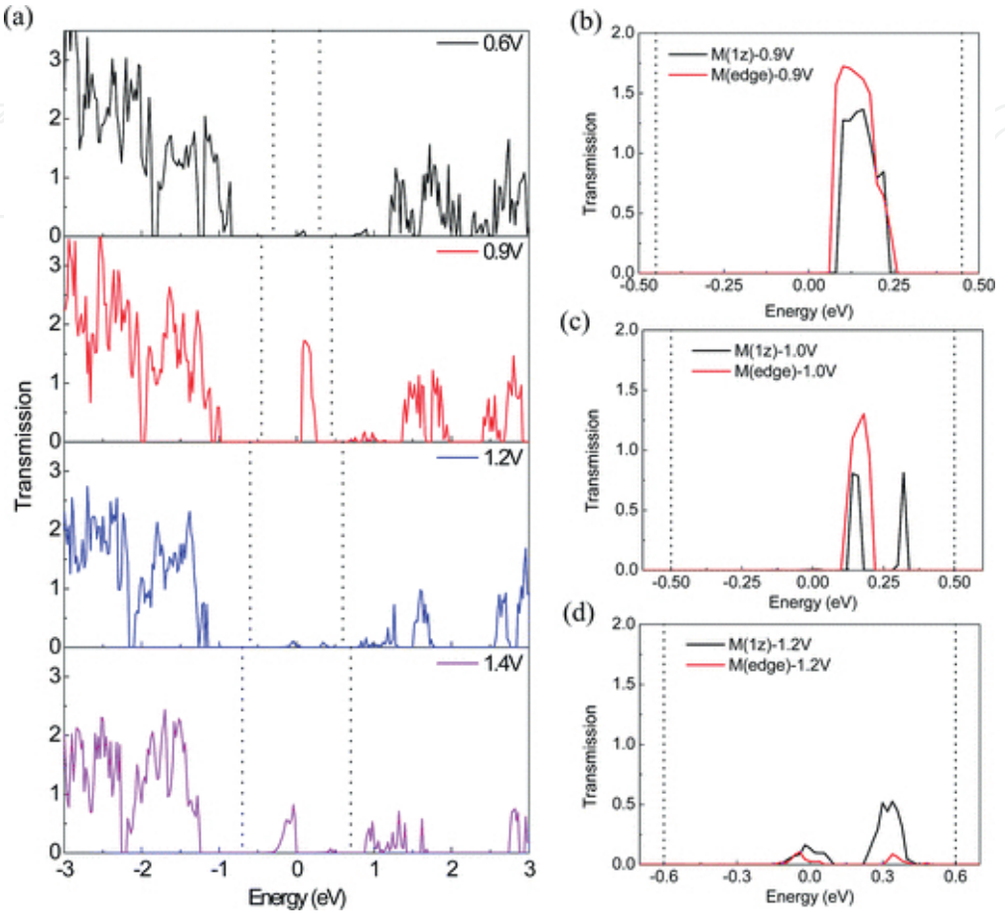

Figure 16. (a) Transmission spectrum for M(edge) at four bias voltages. Dotted line represents the bias window. Transmission spectrum (b) at 0.9 V bias, (c) at 1.0 V bias and (d) at 1.2 V bias for M(1z) and M(edge).

4. Conclusion

First-principles DFT and non-equilibrium Green function calculations have been used to study the electronic properties of the graphene-like 2D materials. It was found that zBPNRs exhibited a non-magnetic direct bandgap semiconducting property and bandgap was about 1 eV. We also found that when the width of zBPNRs increases, the bandgap decreases below the level of BP monolayer, resulting from electrons transport from the P edge to the B edge of the zBPNRs. Moreover, a heterostructure, which consists of a zBPNR and two zSiCNRs, was constructed and the electron transport property was studied. For these zSiC-BP-SiC two-probe devices, a significant NDR effect was observed, arising from the change in the SiC-BP coupling under various biases, and when changing the length of zBPNR, the NDR effect of these

heterostructures can be modulated. In addition, we also studied the electron transport properties of a diode-like structure consisting of the zigzag BP and SiC nanoribbon. For these zBP-SiC two-probe devices, the NDR effect weaken with the increasing width of ribbon, and zBPNRs played an important role in these heterostructures.

For all the armchair MoS_2/WS_2NRs heterostructures, they are found to be a direct bandgap semiconductor. When enlarging the width of WS_2NR, bandgap of these heterostructures narrows slightly, which leads to the current increasing fast and owning a higher current peak. Moreover, when the width of the WS_2NR increases, for the case of M(na) with the interfaces along the zigzag directions, the NDR effect becomes a little better, while for M(nz) with the interfaces along the armchair directions, the NDR effect becomes inferior but with a higher current peak. Interestingly, for M(edge) with W atoms doping on the edges, it not only exhibits a significant NDR effect but also a fast current transport. Therefore, M(edge) may possess the great potential for the application in logic transistor.

Author details

Hui Li[1*], Yi Zhou[1] and Jichen Dong[2]

*Address all correspondence to: lihuilmy@hotmail.com

1 Key Laboratory for Liquid-Solid Structural Evolution and Processing of Materials, Ministry of Education, Shandong University, Shandong, China

2 Department of Mechanical and Biomedical Engineering, City University of Hong Kong, Kowloon Tong, Hong Kong

References

[1] Ritter, K. A., Lyding, J. W. The influence of edge structure on the electronic properties of graphene quantum dots and nanoribbons. Nat. Mater. 2009;8:235–242.

[2] Shen, L., Zeng, M. G., Yang, S. W., Zhang, C., Wang, X. F., Feng,Y. P. Electron transport properties of atomic carbon nanowires between graphene electrodes. J. Am. Chem. Soc. 2010;132:11481–11486.

[3] Mativetsky, J. M., Liscio, A., Treossi, E., Orgiu, E., Zanelli, A.,Samorì, P., et al. Graphene transistors via in situ voltage-induced reduction of graphene-oxide under ambient conditions . J. Am. Chem. Soc. 2011;133:14320–14326.

[4] Westervelt, R. M. Graphene nanoelectronics. Science. 2008;320:324–325.

[5] Novoselov, K. S., Geim, A. K., Morozov, S. V., Jiang, D., Zhang, Y., Dubonos, S. V., et al. Electric field effect in atomically thin carbon films. Science. 2004;306:666–669.

[6] Chen, J. -H., Jang, C., Xiao, S., Ishigami, M., Fuhrer, M. S. Intrinsic and extrinsic performance limits of graphene devices on SiO_2. Nat. Nanotech. 2008;3:206-209.

[7] Chen, F., Xia, J., Ferry, D. K., Tao, N. Dielectric screening enhanced performance in graphene FET. Nano Lett. 2009;9:2571–2574.

[8] Lin, Y. M., Dimitrakopoulos, C., Jenkins, K. A., Farmer, D. B., Chiu, H. Y., Grill, A., et al. 100-GHz transistors from wafer-scale epitaxial graphene. Science. 2010;327:662–662.

[9] Hollander, M. J., LaBella, M., Hughes, Z. R., Zhu, M., Trumbull, K. A., Cavalero, R., et al. Enhanced transport and transistor performance with oxide seeded high-κ gate dielectrics on wafer-scale epitaxial graphene. Nano Lett. 2011;11:3601–3607.

[10] Liao, L., Bai, J. W., Qu, Y. Q., Lin, Y. C., Li, Y. J., Huang, Y., et al. High-K oxide nanoribbons as gate dielectrics for high mobility topgated graphene transistors. Proc. Natl. Acad. Sci. U.S.A. 2001;107:6711–6715. [14] 6

[11] Elias, D. C., Gorbachev, R.V., Mayorov, A.S., Zhukov, A.A., Blake, P., Ponomarenko, L.A., et al. Dirac cones reshaped by interaction effects in suspended graphene. Nat. Phys. 2011;7:701–704.

[12] Mayorov, A. S., Gorbachev, R.V., Morozov, S.V., Britnell, L., Jalil, R., Ponomarenko, L.A., et al. Micrometer-scale ballistic transport in encapsulated graphene at room temperature. Nano Lett. 2011;11:2396–2399.

[13] Castro Neto, A. H., Guinea, F., Peres, N. M. R., Novoselov, K. S., Geim, A. K. The electronic properties of graphene. Rev. Mod. Phys. 2009;81:109–162. 2

[14] Li, X., Cai, W. W., An, J. H., Kim, S. Y., Nah, J., Yang, D. X., et al. Large-area synthesis of high-quality and uniform graphene films on copper foils. Science. 2009;324:1312–1314. 7

[15] Balog, R., Jørgensen, B., Nilsson, L., Andersen, M., Rienks, E., Bianchi, M., et al. Bandgap opening in graphene induced by patterned hydrogen adsorption. Nat. Mater. 2010;9:315–319.

[16] Gan, L., Zhou, J., Ke, F., Gu, H., Li, D. N., Hu, Z. H., et al. Tuning the properties of graphene using a reversible gas-phase reaction. NPG Asia Mater. 2012;4(11):e31

[17] Zhang, W. J., Lin, C. T., Liu, K. K., Tite, T., Su, C. Y., Chang, C. H., et al. Opening an electrical band gap of bilayer graphene with molecular doping. ACS Nano. 2011;5:7517–7524.

[18] Dong, J.C., Li, H. Monoatomic layer electronic constructed by granphene and boron nitride nanoribbons. J. Phys. Chem. 2012;116:17259–17267.

[19] Zhang, Y., Tang, T.-T., Girit, C., Hao, Z., Martin, M.C., Zettl, A., et al. Direct observation of a widely tunable bandgap in bilayer graphene. Nature. 2009;459:820–823.

[20] Castro, E. V., Novoselov, K. S., Morozov, S. V., Peres, N. M. R., Lopes dos Santos, J. M. B., Nilsson, J., et al. Biased bilayer graphene: semiconductor with a gap tunable by the electric field effect. Phys. Rev. Lett. 2007;99:216802–216805.

[21] Ohta, T., Bostwick, A., Seyller, T., Horn, K., Rotenberg, E. Controlling the electronic structure of bilayer graphene. Science. 2006;313:951–954.

[22] Zhang, Y. B., Tang, T. T., Girit, C., Hao, Z., Martin, M. C., Zettl, A., et al. Direct observation of a widely tunable bandgap in bilayer graphene. Nature. 2009;459:820–823.

[23] Li, X., Wang, X., Zhang, L., Lee, S., Dai, H. Chemically derived, ultrasmooth graphene nanoribbon semiconductors. Science. 2008;319:1229–1232.

[24] Son, Y. W., Cohen, M. L., Louie, S. G. Energy gaps in graphene nanoribbons. Phys. Rev. Lett. 2006;97:216803–216806.

[25] Hicks, J., Tejeda, A., Taleb-Ibrahimi, A., Nevius, M. S., Wang, F., Shepperd, K., et al. A widebandgap metal-semiconductor-metal nanostructure made entirely from graphene. Nat. Phys. 2013;9:49–54.

[26] Alejandro, L. C. Prediction of boron-phosphorous nanographene-like material. Int. J. Quantum Chem. 2012;112:3152–3157.

[27] Zhang, H., Li, X.-B., Liu, L.-M. Tunable electronic and magnetic properties of WS2 nanoribbons. J. Appl. Phys. 2013;114:093710.

[28] Chhowalla, M., Shin, H. S., Eda, G., Li, L.-J., Loh, K. P., Zhang, H. The chemistry of two-dimensional layered transition metal dichalcogenide nanosheets. Nat. Chem. 2013;5:263.

[29] Zhang, H., Liu, L.-M., Lau, W.-M. Dimension-dependent phase transition and magnetic properties of VS_2. J. Mater. Chem. A. 2013;1:10821.

[30] Wilson, J. A., Yoffe, A. D. The transition metal dichalcogenides discussion and interpretation of the observed optical, electrical and structural properties. Adv. Phys. 1969;18:193–335.

[31] Fivaz, R., Mooser, E. Mobility of charge carriers in semiconducting layer structures. Phys. Rev. 1967;163:743–755.

[32] Radisavljevic, B., Radenovic, A., Brivio, J., Giacometti, V., Kis, A. A. Single-layer MoS_2. Nat. Nanotechnol. 2011;6:147–150.

[33] Ye, J. T., Zhang, Y. J., Akashi, R., Bahramy, M. S., Arita, R., Iwasa, Y. Superconducting dome in a gate-tuned band insulator. Science. 2012;338:1193–1196.

[34] Withers, R. L., Wilson, J. A. An examination of the formation and characteristics of charge-density waves in inorganic materials with special reference to the two and one-dimensional transition-metal chalcogenides. J. Phys. C. 1986;19:4809–4845.

[35] Liu, H., Neal, A. T., Ye, P. D. Channel length scaling of MoS_2 MOSFETs. ACS Nano. 2012;6:8563–8569.

[36] Radisavljevic, B., Kis, A. A. Mobility engineering and a metal–insulator transition in monolayer MoS_2. Nat. Mater. 2013;12:815–820.

[37] Verble, J. L., Wietling, T. J., Reed, P. R. Rigid-layer lattice vibrations and Van der Waals bonding in hexagonal MoS2. Solid State Commun. 1972;11:941–944.

[38] Novoselov, K. S., Jiang, D., Schedin, F., Booth, T. J., Khotkevich, V. V., Morozov, S. V., et al. Two-dimensional atomic crystals. Proc. Natl. Acad. Sci. U.S.A. 2005;102:10451–10453.

[39] Coleman, J. N., Lotya, M., O'Neill, A., Bergin, S. D., King, P. J., Khan, U., et al. Two-dimensional nanosheets produced by liquid exfoliation of layered materials. Science. 2011;331:568–571.

[40] Wang, Z., Li, H., Liu, Z., Shi, Z., Lu, J., Suenaga, K., et al. Mixed low-dimensional nanomaterial: 2D ultranarrow MoS_2 inorganic nanoribbons encapsulated in quasi-1D carbon nanotubes. J. Am. Chem. Soc. 2010;132:13840–13847.

[41] Liu, X., Xu, T., Wu, X., Zhang, Z., Yu, J., Qiu, H., et al. Top–down fabrication of sub-nanometre semiconducting nanoribbons derived from molybdenum disulfide sheets. Nat. Commun. 2013;4:1776.

[42] Liu, Z., Suenaga, K., Wang, Z., Shi, Z., Okunishi, E., Iijima, S. Identification of active atomic defects in a monolayered tungsten disulphide nanoribbon. Nat. Commun. 2013;2:213.

[43] Nethravathi, C., Anto Jeffery, A., Rajamathi, M., Kawamoto, N., Tenne, R., Golberg, D., et al. Chemical unzipping of WS2 nanotubes. ACS Nano. 2013;7:7311–7317.

[44] Zhu, Z. Y., Cheng, Y. C., Schwingenschlögl, U. Giant spin-orbit-induced spin splitting in two-dimensional transition-metal dichalcogenide semiconductors. Phys. Rev. B. 2011;84:153402.

[45] Jiang, H. Electronic band structures of molybdenum and tungsten dichalcogenides by the GW approach. J. Phys. Chem. C. 2012;116:7664.

[46] Ramasubramaniam, A. Large excitonic effects in monolayers of molybdenum and tungsten dichalcogenides. Phys. Rev. B. 2012;86:115409.

[47] Feng, W., Yao, Y., Zhu, W., Zhou, J., Yao, W., Xiao, D. Intrinsic spin Hall effect in monolayers of group-VI dichalcogenides: a first-principles study. Phys. Rev. B. 2012;86:165108.

[48] Gutierrez, H.R., Perea-López, N., Elías, A.L., Berkdemir, A., Wang, B., Lv, R., et al. Extraordinary room-temperature photoluminescence in triangular WS2 monolayers. Nano Lett. 2013;13:3447–3454.

[49] Brandbyge, M., Mozos, J. L., Ordejon, P., Taylor, J., Stokbro, K. Density-functional method for nonequilibrium electron transport. Phys. Rev. B. 2002;65:165401–165417.

[50] ATK. QuantumWise. Copenhagen, Denmark. www.quantumwise.com [Internet]. 2008.

[51] Sun, L., Li, Y. F., Li, Z. Y., Li, Q. X., Zhou, Z., Chen, Z. F., et al. Electronic structures of SiC nanoribbons. J. Chem. Phys. 2008;129:174114–174117.

[52] Park, C. H., Louie, S. G. Energy gaps and stark effect in boron nitride nanoribbons. Nano Lett. 2008;8:2200–2203.

[53] Lou, P., Lee, J. Y. Band structures of narrow zigzag silicon carbon nanoribbons. J. Phys. Chem. C. 2009;113:12637–12640.

[54] Li, Z. Y., Qian, H. Y., Wu, J., Gu, B. L., Duan, W. H. Role of symmetry in the transport properties of graphene nanoribbons under bias. Phys. Rev. Lett. 2008;100:206802.

[55] Lu, W. C., Meunier, V., Bernholc, J. Nonequilibrium quantum transport properties of organic molecules on silicon. Phys. Rev. Lett. 2005;95:206805.

[56] Qi, J. S., Huang, J. Y., Feng, J., Shi, D. N., Li, J. The possibility of chemically inert, graphene-based all-carbon electronic devices with 0.8 eV gap. ACS Nano. 2011;5:3475–3482.

[57] Zheng, X. H., Lu, W. C., Abtew, T. A., Meunier, V., Bernholc, J. Negative differential resistance in C60-based electronic devices. ACS Nano. 2010;4:7205–7210.

[58] Gong, Y., Lin, J., Wang, X., Shi, G., Lei, S., Lin, Z., et al. Vertical and in-plane heterostructures from WS2/MoS2 monolayers. Nat. Mater. 2014;13:1135–1142.

IntechOpen